ISSN 0915-633X

NATIONAL INSTITUTE FOR FUSION SCIENCE

A Compact Neutron Counter Telescope with Thick Radiator (Cotetra) for Fusion Experiment

M. Osakabe, S. Itoh, Y. Gotoh, M. Sasao and J. Fujita

(Received – Dec. 14, 1992)

NIFS-205

Jan. 1993

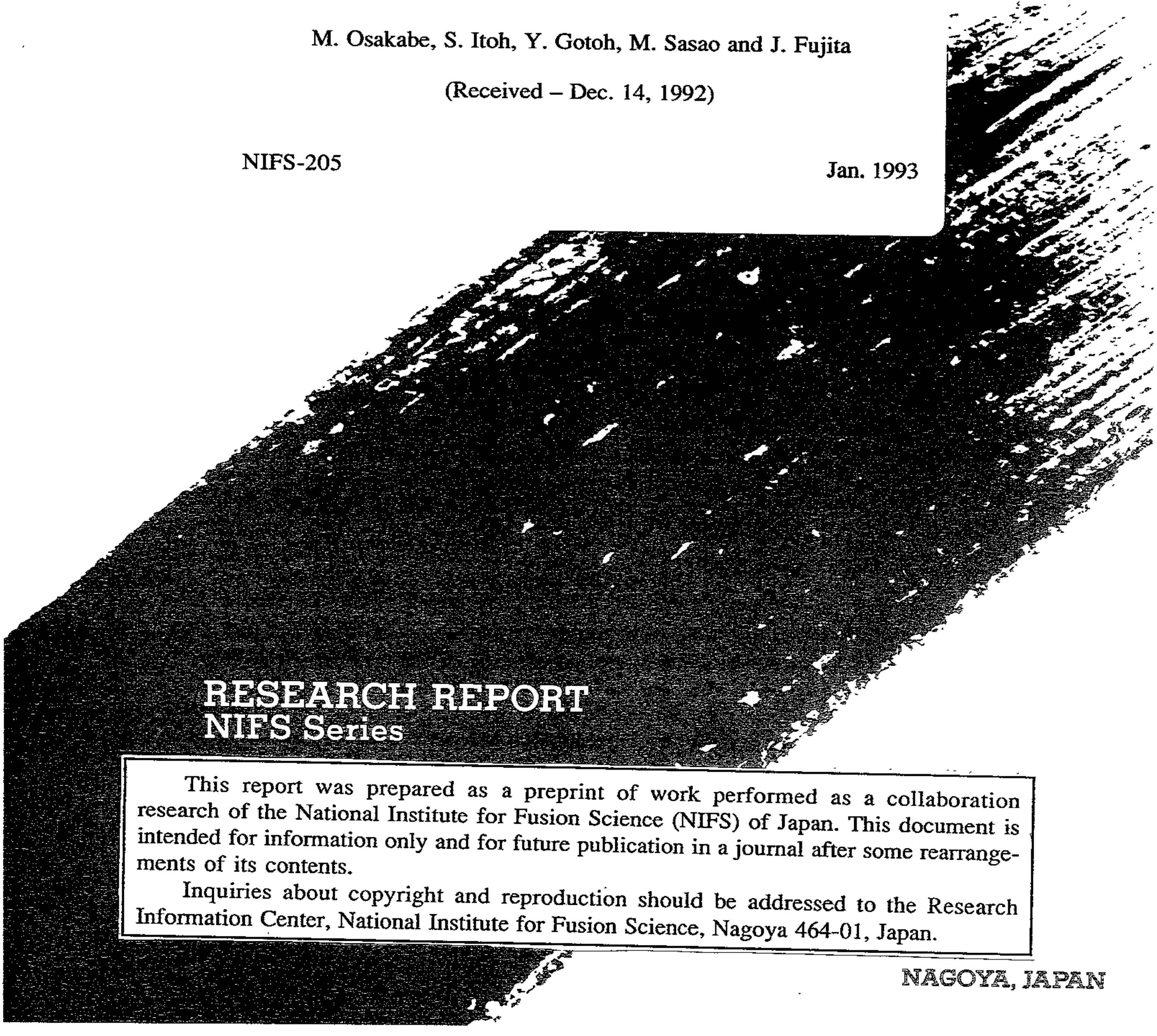

RESEARCH REPORT
NIFS Series

This report was prepared as a preprint of work performed as a collaboration research of the National Institute for Fusion Science (NIFS) of Japan. This document is intended for information only and for future publication in a journal after some rearrangements of its contents.

Inquiries about copyright and reproduction should be addressed to the Research Information Center, National Institute for Fusion Science, Nagoya 464-01, Japan.

NAGOYA, JAPAN

A COMPACT NEUTRON COUNTER TELESCOPE WITH THICK RADIATOR (COTETRA) FOR FUSION EXPERIMENT

M.OSAKABE, S.ITOH[*1], Y.GOTOH[*1]
M.SASAO[*2], J.FUJITA[*2]

Department of Fusion Science
School of Mathematical and Physical Science
The Graduate University for Advanced Studies
Nagoya 464-01, Japan

[*1] Department of Nuclear Engineering
School of Engineering
Nagoya University
Nagoya 464-01, Japan

[*2] National Institute for Fusion Science (NIFS)
Nagoya 464-01, Japan

Keywords : DT neutron, neutron energy spectrum, neutron energy spectrometer, recoil proton telescope, plastic scintillator, plasma diagnostics, neutron diagnostics, ion temperature

Abstracts

A new type of neutron spectrometer, based on recoil proton measurement, has been developed for diagnosing a DT fusion plasma. This spectrometer has such advantages as: 1. direct measurement of the neutron energy without the unfolding procedure, 2. relatively high detection efficiency for 14 MeV neutrons, 3. a wide dynamic range of counting rate, and 4. perfect n-γ discrimination. To examine the performance of this spectrometer, we developed a Monte Carlo simulation code. It predicts that we may achieve energy resolution up to 3% with a detection efficiency of 10^{-5} [count cm^2/n] if we could successfully adjust the condition of the spectrometer. A prototype spectrometer was constructed and was compared with the Monte Carlo prediction. The energy resolution of 5.3±0.7% for 14 MeV neutron was obtained for the prototype spectrometer and the calculation agrees with the experimental results within its margin of error if we take into account the intrinsic energy resolution of the detector that is used in the prototype.

1. Introduction

A number of diagnostic systems have been developed and applied to plasma experiments on magnetically confined fusion devices. Among them, neutron measurement gives information about the fusion output, the behaviors of fast fusion product particles, ion temperatures, deuteron density and so on [1-3]. In DT burning experiments, many conventional diagnostic devices will suffer from the neutron and gamma ray irradiation, and therefore the role of neutron diagnostics becomes more important [4].

Plasma parameters obtainable from neutron spectrum measurement depends on its energy resolution (ΔR). When it is measured with high resolution, we can determine the plasma ion temperature, T_i from the Doppler width, ΔE_D, of the DT neutron peak by using the relation of $T_i \simeq (\Delta E_D/177)^2$, where Ti and ΔE_D are in [keV]. Generally in large tokamaks such as JT-60U, JET and TFTR, the ion temperature of the plasma is about 5 to 30 keV. Therefore, the required ΔR of a spectrometer is about 3% at the DT neutron energy. Even if the energy resolution of the spectrum is not fine enough to determine T_i, the total amount of neutron yield and the spatial distribution of neutron emission are obtainable, which are also of our great interests. In this case, the energy of the neutron is measured in order to identify its origin of the reaction, e.g., DT reaction, DD reaction, or (γ, n) reaction etc.

The time resolution is another important parameter of the measurement since the plasma parameters are changing with time. Because the slowing-down time of 3.5 MeV α-particle (τ_α) is one of the most important time scales in the fusion experiment (typically, $\tau_\alpha \geq 10^{-1}$ sec for the electron density less than 3×10^{20} [electrons/m^3] at $T_e = 10$ keV), it is preferable to set the time resolution less than 0.1 sec. In order to get enough count ($\geq 10^2$ counts) during this period, the count rate capability (C^{cap}) of the spectrometer should be greater than 10^3 cps. In the DT experiment at TFTR and JET, the DT neutron flux of $10^8 \sim 10^{10}$ n/sec·cm^2 is expected at the place where the neutron spectrometer is located. To obtain the count rate over 10^3 cps, the detection efficiency (η) of the spectrometer must be greater than 10^{-5} count·cm^2/n.

Therefore, the required performances of the neutron spectrometer for DT plasma diagnostics are $\Delta R<3\%$, $\eta>10^{-5}$ count·cm^2/n, and $C^{cap}>10^3$ cps.

To satisfy these conditions, a modified recoil counter telescope was developed. In a conventional recoil counter telescope, a thin polyethylene film is used as a radiator. In the present spectrometer, this thin film (~10μm) was replaced with relatively thick scintillator (2mm) and the energy deposit of a recoil proton in the radiator was measured. With this modification, the detection efficiency was increased without deteriorating the energy resolution of the spectrometer. The idea is similar to that of the spectrometer being suggested by Mozley et.al.[8] and constructed by Calvert et al.[9] and Gellar et.al.[10] in the field of nuclear physics. Gellar used stilbene scintillator as a radiator and this scintillator was coupled with single photomultiplier tube. In the present spectrometer, the NE102A plastic scintillator was used with two photomultiplier tubes so as to increase the count rate capability and to discriminate the noise of PMT signals by coincidence technique.

Actual sizes and costs are other aspects of a spectrometer for a fusion experiment. These are important in measuring neutron emission profiles and ion temperature profiles of a plasma since certain numbers of detectors are needed to achieve a good spatial resolution, and the space around plasma devices to install those detectors is usually quite limited.

In this paper, we show the properties of our spectrometer that were obtained through the calculation and experiment. In Chapter 2, the detection principle is described and the calculated performances of the spectrometer is presented. The experimental results are shown in Chapter 3. Finally, the overall performance are discussed in Chapter 4 and a conclusion is given in Chapter 5.

2 Estimation of the Spectrometer Performances

2.1 Principle of Measurement

The spectrometer consists of two detectors as shown in Fig. 1, where neutrons are coming from the left hand side and enter into the detector #1. Some of protons are recoiled by the incident neutrons and these protons fly to the detector #2. The volume between two detectors is vacuum so that the recoil proton will not lose its energy.

The energy of the incident neutron, E_n, can be expressed by

$$E_n = E_p \sec^2\theta, \qquad (1)$$

where E_p represents the energy of the recoil proton and θ is the recoil angle with respect to the incident neutron direction. The recoil proton loses a part of its energy in detector #1, E_1, and the rest in detector #2, E_2. Then,

$$E_p = E_1 + E_2. \qquad (2)$$

As can be seen in Fig. 1, the recoil angle of the proton that enters into detector #2 is limited by the sizes of detector #1 and #2 and by the distance(ℓ) between them. This limitation can be expressed as

$$0 \leq \theta \leq \arctan\{(r_1+r_2)/\ell\}, \text{ or} \qquad (3)$$

$$1 \leq \sec^2\theta \leq 1+\{(r_1+r_2)/\ell\}^2, \qquad (4)$$

where r_1 and r_2 are radii of detector #1 and detector #2. If we choose $r_1+r_2 << \ell$, we get $\sec^2\theta \simeq 1$. In this case, Eq.(1) becomes $E_p \simeq E_n$. Using this relation and eq.(2), we get

$$E_n \simeq E_1 + E_2 \qquad (2)'$$

2.2 Energy Resolution

Energy resolution of the present spectrometer can be expressed as follows

$$\Delta E_{tot}{}^2 = \Delta E_{det}{}^2 + \Delta E_{geo}{}^2 \qquad (5)$$

$$\Delta E_{det}{}^2 = \langle \Delta E_1{}^2 \rangle_{12} + \langle \Delta E_2{}^2 \rangle_{12}, \qquad (6)$$

where ΔE_{tot} is total energy resolution of the spectrometer. ΔE_{det} is energy broadening due to the intrinsic energy resolution of detector #1 and #2, and ΔE_{geo} that due to the geometrical configuration. $\langle\rangle_{12}$ denotes an average over the distribution of (E_1,E_2), which can be obtained from the calculation described in chapter 2. The energy resolution of each detector (ΔE_i, i=1,2) at a certain energy is considered to be proportional to the square root of the energy deposit (E_i, i=1,2) in each detector, i.e,

$$\Delta E_i = \alpha_i \cdot (E_i)^{1/2}, \qquad (7)$$

where α_i is a parameter determined by calibration experiments, using internal conversion electron from ^{137}Cs and ^{207}Bi. The result are shown in table 1.

There are two types of geometrical effects that appear in the energy resolution. One depends mainly on the ratio $(r_1+r_2)/\ell$ and appears in the second term of the eq. (5). This effect strongly relates to the restriction on the recoil angle by the configuration of the spectrometer. Another effect depends on the thickness of detector #1, d_1. This effect appears in the first term of eq. (5) through the distribution of (E_1, E_2), especially when the energy of the incident neutron is relatively low.

2.3 Detection Efficiency

Total detection efficiency of the spectrometer, η_{tot} [count·cm^2/n], is the product of the neutron detection efficiency of the detector #1, η_1 [count·cm^2/n], and the geometrical efficiency, ε_{geo},

$$\eta_{tot} = \eta_1 \cdot \varepsilon_{geo}. \tag{8}$$

Here, ε_{geo}, the probability that a recoil proton is detected in the detector #2, was determined by a Monte Carlo calculation. η_1 can be calculated by

$$\eta_1 = S_1 \cdot \Sigma_p \cdot \{1-\exp(-\Sigma_t \cdot d_1)\}/\Sigma_t \tag{9}$$

$$\Sigma_p = n_H \sigma_{pH}(E) \tag{10}$$

$$\Sigma_t = n_H \sigma_{tH}(E) + n_C \sigma_{tC}(E) \tag{11}$$

where S_1 :area of detector #1 ($=\pi r_1^2$ [cm^2])

d_1 :thickness of detector #1

$\Sigma_p(E)$:macroscopic cross section for (n, p) scattering of the detector #1

$\Sigma_t(E)$:macroscopic total cross section of the detector #1

$\sigma_{pH}(E)$:microscopic cross section for (n, p) scattering of Hydrogen atom

$\sigma_{ti}(E)$:microscopic total cross section of nuclide i (where i= C,H)

n_i :density of nuclide i in detector #1

Similar to the energy resolution, the thickness of d_1 and the ratio $(r_1+r_2)/\ell$ affect on the detection efficiency and their influences appear in η_1 and ε_{geo}, respectively.

2.4 Monte Carlo Calculation

Based on the principles described above, we developed a Monte Carlo calculation code that simulates the detection process of the spectrometer. Using this code, it is possible to estimate the energy resolution and the detection efficiency, and consequently to choose a suitable configuration for various purposes.

The calculational model is shown in Fig. 2. The thickness (d_1) and the distance (ℓ) are varied in the calculations. The other parameters, such as d_2, r_1 and r_2, are fixed as shown in table 2. 'Japanese Evaluated Nuclear Data Library version 3', JENDL3, is used as a neutron cross section data set.

The results of the calculation are shown in Fig. 3. The total energy resolution, ΔE_{tot}, and the detection efficiency, η_{tot}, are expressed with contours in these figures. In general, the total resolution and the detection efficiency increase as d_1 increases and as ℓ decreases. Both ΔE_{tot} and η_{tot} do not change with d_1 when d_1 is larger than ~2mm. This length is equivalent to the range of 14.1MeV proton in NE102A. When the thickness of the detector #1 is larger than the range of the recoil proton, there exists a 'Dead Region'. Protons produced here cannot reach the detector #2. As these protons only generate accidental coincidence signals, the thickness of the detector #1 should be chosen carefully in accordance with the energy range of the neutron that we are interested in.

The increase of ΔE_{tot} with d_1 is due to the increase of the average ratio of E_1 to E_p, $\langle E_1/E_p \rangle_{12}$, because the energy resolution of detector #1 is much worse than that of detector #2 in the calibration done here. This average ratio expresses the amount of the contribution of detector #1 to the total energy resolution of the spectrometer.

It can be seen in Fig.3(a) that the present spectrometer fulfills the requirement of the total detection efficiency for fusion neutron measurement, i.e. $\eta_{tot.} > 10^{-5}$ [counts·cm^2/n], at any point of the calculated region. It also satisfies the requirement of the energy resolution, i.e., $\Delta E_{tot}/E \leq 3\%$, in a subregion of Fig.3(b). From these figures, we can conclude that the thickness (d_1) ~0.8mm and the distance (ℓ) ~200mm are the best choice for our purpose.

3. Experiment

A prototype spectrometer was constructed and tested using an intense deuterium-tritium neutron source at Osaka University in Japan (OKTAVIAN). Monoenergetic neutrons (fwhm$\simeq$3%) of an average energy of 14.8MeV on the zero degree line were used. The spectrometer was placed on the line at a distance of 141 cm from the target (see Fig. 4). To monitor the flux and energy spectrum of the neutrons at this angle, several kinds of activation foils (Al, Ni and Nb) and 'time-of-flight' (TOF) neutron monitor (NE213) were placed at a distance of 21 cm and 646cm from the target, respectively.

3.1 Prototype Spectrometer

Figure 5 shows a schematic drawing of the prototype spectrometer assembly. A plastic scintillator (NE102A) and a Si(Li) semiconductor detector were used as the detector #1 and #2, respectively. The sizes of these detectors are shown in the table 3.

The plastic scintillator was installed in an aluminum cylinder with inner polished surface (hollow light guide) and was optically connected to two photomultiplier tubes through it. These two photomultiplier tubes (HAMAMATSU RB329-02) were placed to face the cylindrical side surface of the scintillator so that they would not disturb the incident neutrons and the recoil protons. Since the photo tubes did not directly see the right hand side flat surface of the scintillator in Fig.5, this side was coated with the evaporated aluminum in order not to lose the right going scintillation light and to shield the second detector, optically. On the left hand side flat surface of the scintillator, a Lucite lens was attached to extract the scintillation light effectively to outside from the scintillator [10].

3.2 Electronics System

Fig. 6 shows the block diagram of the electronics system. The signal of the detector #1 was obtained via two photomultiplier tubes, where the fast coincidence technique was applied to eliminate PMT noises. The bias voltage of photomultiplier tubes was adjusted so that the linear signals of them would have the same pulse height for the Compton edge of ^{137}Cs gamma ray. Gate signals for true events were generated by the SCA output of TAC, which analyzed the time difference between timing signals of the detector #2 and the coincidence signals of fast outputs from two photomultipliers of the detector #1. The time differences (ΔT) between the signal from the detector #1 and that from the pick-up ring of the accelerator were measured to distinguish the neutron events from that of target gamma rays.

The time difference signals (ΔT) and the linear signals of the detector #1 and #2 (L_1 and L_2) were digitized by three CAMAC ADCs (LeCroy 3512) using a 'event-by-event' mode. These data were stored in the vector form of (L_1,L_2,ΔT) in a personal computer (NEC PC9801).

The counting rate of detector #1, CR_1, after the coincidence of two photo tubes, and the coincidence event rate of the detector #1 and #2, CR_{co}, were recorded by scalars and was used to estimate the detection efficiency and accidental coincidence rate.

The zero offsets of the electronic system in the L_1 and L_2 signals were determined by using a mercury pulser.

3.3 Experimental Result

The monoenergetic neutron events are expected to appear on a specific linear line in an E_1-E_2 plane due to the relation of eq.(2). Figure 7 shows an example of (L_1,L_2) distribution obtained in our experiment. In Fig.7(a), events due to the DT neutrons appear around a line ℓ with a certain broadening of $\Delta L(L_1, L_2)$. This broadening was mainly caused by the intrinsic energy resolutions of the detector #1 and #2.

The data shown in Fig.7(a) includes all events, i.e. the events due to the target γ-ray, the accidental coincidence and the true events. Most of the events due to the target γ-ray can be discriminated by the ΔT signal. Fig. 8 shows the histogram of ΔT. In this figure, the right peak and the left peak correspond to the events of the target γ-rays and those of the DT neutrons, respectively. Fig.7(b) and (c) shows the distribution of (L_1,L_2) due to the γ-ray and neutron, respectively. The γ-ray events concentrate around the lower left side corner of the distribution because the detector #1 and #2 do not have enough thickness for γ-rays and Compton electrons to lose large amount of their energy. This is a big advantage of our spectrometer. Using this feature, we can easily discriminate the γ-ray events from the DT neutron events without using the ΔT signal.

To determine the effect of accidental coincidence, the background run was also performed, where a Ta plate was placed between detector #1 and #2. Fig. 7(d) shows the result of background run, where the γ-ray events identified by the ΔT signal are removed.

Figure 9 shows the one dimensional pulse height spectrum (PHS) that is obtained by projecting the points in Fig. 7 onto the vertical axis (L_2-axis) along the line ℓ. The pulse height spectra shown in this figure are normalized with the measurement time and, moreover, that of the background run is normalized by the count rate of detector #1 so that it has same source intensity as the foreground run does. The zero points of the electronic system are also projected onto L_2-axis and they locate at -2.78 ± 0.04 [ch.] in these figures. Fig. 9-(c) shows the PHS due to the true events, which is obtained by the subtraction of the background PHS from the foreground PHS.

Measuring the 5.45MeV α-ray from ^{241}Am by Si(Li) detector, the energy calibration data was obtained. In Fig. 9-(c), 49.1 channel corresponds to the energy of 5.45MeV.

4. Discussion

4.1 Energy Resolution of the Prototype Spectrometer

From the TOF measurement of the neutron between the T target and the NE213 detector, it is observed that the energy of the neutron on the 0 degree line is about 14.8MeV. This agrees with the theoretical prediction. Therefore, the peak position of the PHS in Fig. 9-(c) is set to be 14.8MeV. By using this result and the projected zero points, this PHS is transformed to the neutron energy spectrum as shown in Fig.10. Here, vertical axis is in the unit of [n/cm^2·sec·MeV], which includes 'dead time' correction factor of ADC and efficiency correction factor calculated with the Monte Carlo code as shown in Fig.11. In this figure, the DT neutron peak locates at 14.8±0.1MeV. If we calibrate the horizontal axis of the PHS with the peak position of the 5.45 MeV α-ray, the DT neutron peak appears at 3% lower. The difference is likely attributable to lack of calibration data point or its too low pulse height.

The FWHM of the DT peak in Fig.10 is 0.91±0.10MeV, i.e. 6.1±0.7%. Considering that the energy broadening of the source neutron was about 3.0±0.4% [11] in this kind of experiment, the total energy resolution of the prototype spectrometer is 5.3±0.9%. This agrees with the Monte Carlo prediction (5.2%.) within its experimental error.

In the prototype configuration, the restriction on the recoil angle of the proton being detected is so tight that the contribution of ΔE_{geo} to ΔE_{tot} can be neglected and the total energy resolution of the spectrometer (ΔE_{tot}) is determined only by the intrinsic energy resolution of the detector #1 and #2 (ΔE_{det}) as shown in Fig.12. Since the contribution of ΔE_{geo} to ΔE_{tot} is small enough when the distance ℓ is longer than 180mm, this can be shorten to increase the detection efficiency without disturbing the total energy resolution.

4.2 Detection Efficiency of the Prototype Spectrometer

The performances of the prototype spectrometer are summarized in table 4. The experimental detection efficiencies in this table were calculated from the count rates (CRs) and the neutron flux (ϕ) using the following equations:

$$\eta_{tot} = CR_{co}^{true} / \phi \qquad (12)$$

$$\eta_1 = CR_1^{true} / \phi \qquad (13)$$

$$\varepsilon_{geo} = CR_{co}^{true} / CR_1^{true} \qquad (14)$$

where the neutron flux (ϕ) was measured using the activation foil and was $(2.6\pm0.2)\times10^3$ [n/cm^{2}sec] at the place where the spectrometer was placed. Using the count rate and the coincidence rate at the foreground and background run, the count rate due to the true events (CR_1^{true}, CR_{co}^{true}) can be expressed as follows:

$$CR_1^{true} = r_n^{fore} \cdot CR_1^{fore} \qquad (15)$$

$$CR_{co}^{true} = r_n^{fore} \cdot CR_{co}^{fore} - f \cdot r_n^{back} \cdot CR_{co}^{back}. \qquad (16)$$

Here, the neutron ratio, r_n, is the ratio of the neutron events to total events and is obtained from the data shown in Fig. 8. Together with r_n, the count rate of detector #1(CR_1) and the coincidence rate between detector #1 and #2(CR_{co}) are shown in table 5. The correction factor (f), which eliminates the effect on the accidental coincidence rate due to the source intensity difference between foreground and background run, can be expressed:

$$f = (CR_1^{fore} / CR_1^{back})^2 \qquad (17)$$

The detection efficiencies shown in table 4 agree with the Monte Carlo prediction within its margin of error. These agreements in the detection efficiency and the energy resolution prove that the Monte Carlo Calculation is proceeded appropriately.

Since the distance ℓ can be shorten to 180mm without deteriorating the energy resolution of the spectrometer, the detection efficiency of the prototype can be increased to 2.8×10^{-4} [count·cm^2/n] as shown in Fig. 12.

4.3 Count Rate Capability of the Prototype Spectrometer

The count rate capability of the whole spectrometer system (C_{tot}^{cap}) is determined by the product of the count rate capability of the detector #1 (C_1^{cap}) and the geometrical detection efficiency (ε_{geo}):

$$C_{tot}^{cap} = C_1^{cap} \cdot \varepsilon_{geo} \qquad (18)$$

In the prototype spectrometer, C_1^{cap} depends on the count rate capability of the NIM module and is about 10^5 cps. Since ε_{geo} is about 10^{-3}, the C_{tot}^{cap} of the present system is about 10^2 cps.

A new spectrometer system, which uses fast NIM modules and has shorter ℓ (=180 mm), is under development. In this new system, the C_1^{cap} is improved to 10^7 cps and ε_{geo} is doubled. Therefore, it is expected that this new system has the total count rate capability of up to 2×10^4 cps, which corresponds to the neutron flux of 10^{+9} [n/cm^2 sec].

5. Conclusion

A new type of neutron spectrometer, based on recoil proton measurement, has been developed. The basic performance of this spectrometer was examined both by the experiment and calculation.

It is confirmed by the Monte Carlo Calculation that this spectrometer can achieve the required performance of the neutron energy spectrometer for the DT plasma diagnostics, i.e. energy resolution $\leq$ 3% and the detection efficiency $\geq 10^{-5}$ [count·cm^2/n] for 14MeV neutron.

A prototype of this spectrometer was constructed and was tested using DT monoenergetic neutron source at Osaka University. The energy resolution of 5.3±0.7 [%] and the detection efficiency of $(1.3 \pm 0.2) \times 10^{-4}$ [count·cm^2/n] were obtained and they agree with the results of the Monte Carlo Calculations within their margin of errors if we take the intrinsic energy resolutions of the detectors which were used in the prototype. The present count rate capability of the spectrometer system is about 10^2 [cps], which are mainly resulted from the performances of the NIM modules. By replacing critical modules to the fast ones and rearranging the geometrical configuration of the prototype, this capability will increase to 10^4 cps, which corresponds to the neutron flux of $\sim 10^9$ [n/cm^{2}sec].

It is observed that the events due to the γ-ray did not affect the spectrum of DT neutron. Therefore, this spectrometer is suitable for the DT plasma diagnostics since a lot of γ-rays are induced by the neutrons during discharges.

Compactness and inexpensiveness are other advantages of the present spectrometer although they were not estimated in this text. Especially for the profile monitoring of plasma, where a lot of spectrometers are expected to be used in a very narrow space, these properties become really important.

Currently, another prototype spectrometer has been under development and planned to install in the coming DT experiment at TFTR.

Acknowledgement

Authors wish to thank Prof. A.Takahashi, Prof. T.Iida, and the staffs of OKTAVIAN at Osaka University for the use of the neutron generator and their hospitality. Continuous encouragement by Prof. K.Nishina and useful discussions with the members of Nishina Laboratory at Nagoya University are also gratefully acknowledged. We wish to thank the members of the Safety and Environmental Research Center at NIFS for their help during the experiment.

References

[1] Harald Enge, Nucl. Instr. Meth., A311(1992)595

[2] D.L.Jassby et al., Phys. Fluids, B3(1991)2308

[3] T.Nishitani, The Journal of the Japan Society of Plasma Science and Nuclear Fusion Research, vol.68 No.1 (1992)6

[4] The JET TEAM, Fusion Energy Production from a Deuterium Tritium Plasma In the JET Tokamak, JET-P(91) 66

[5] O.N.Jarvis et al., Rev. Sci. Instrum. 57(1986)1717

[6] R.F.Mozley et.al., Rev. Sci. Instr. 23(1952)569

[7] J.M.Calvert et al., Proc. Phys. Soc. A68(1955)1017

[8] K.N.Gellar et.al, NIM69(1969)141

[9] M. Osakabe et al, Annual Report of NIFS 1990 (ISSN0917-1185)79

[10] M. Osakabe et al, Annual Report of NIFS 1991 (To be Published)

[11] A.Takahashi, Private Communication

Table 1 Resolution parameter, α, as defined by Eq. (7). In an ideal model, measured parameter α of NE102A that is directly connected to the PMT, and that of SSBD was used for detector #1 and #2, respectively. Here, internal conversion electrons from ^{137}Cs and ^{207}Bi were used for NE102A and α-particle from ^{241}Am were used for SSBD. In the case of prototype spectrometer, the actual value of each parameter was measured for each detector.

	α_1 (detector #1)	α_2 (detector #2)
Ideal	1.38×10^{-1}	3.15×10^{-3}
Prototype	1.91×10^{-1}	1.17×10^{-2}

Table 2 Sizes of the detector #1 and #2 used in the calculation. The thickness (d_1) and the distance (ℓ) are varied from 0.2mm to 3mm and from 100mm to 300mm, respectively.

	detector #1	detector #2
Radius (r) [mm]	20	20
Thickness (d) [mm]	0.2 - 3 (varied)	3

Table 3 The sizes of the prototype spectrometer. The distance between detector #1 and #2 are 280mm. * The radius of detector #2 is estimated from the size of its effective area (= 500mm^2).

	detector #1	detector #2
Type of detector	NE102A scintillator	Si(Li) detector
Radius (r) [mm]	21	12.6*
Thickness (d) [mm]	2	5

Table 4 The performances of the prototype spectrometer for 14.8MeV neutron.

	$\Delta E_{tot}/E$ [%]	η_{tot} [count·cm^2/n]	η_1 [count·cm^2/n]	ε_{geo}
Experiment	5.3±0.7	$(1.3\pm0.2)\times10^{-4}$	$(1.0\pm0.1)\times10^{-2}$	$(1.3\pm0.1)\times10^{-3}$
Calculation	5.2	1.2×10^{-4}	8.9×10^{-2}	1.3×10^{-3}

Table 5 List of CR and r_n. The ratio of neutron events to total events (r_n) are obtained from the data shown in Fig. 8.

	Count Rate of Detector#1 CR_1 [cps]	Coincidence Rate CR_{co} [cps]	neutron ratio: r_n
Foreground run	320.2±0.3	0.46±0.02	0.83±0.03
Background run	330.2±0.3	0.057±0.004	0.78±0.08
True events	265±11	0.34±0.04	-

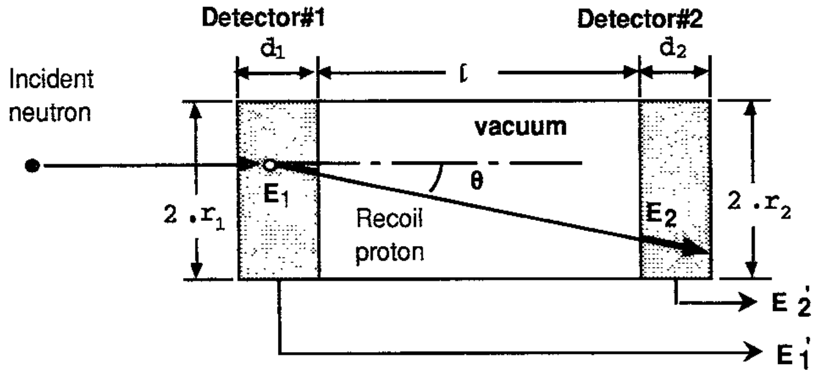

Fig. 1 A Conceptual Figure of the Spectrometer

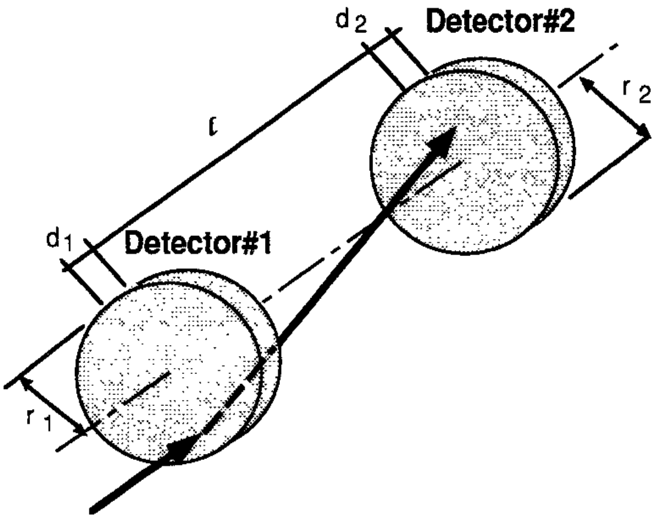

Fig.2 Calculation Model used in the simulation. The effect of the thin aluminum layer and the vacuum region is neglected in this calculation

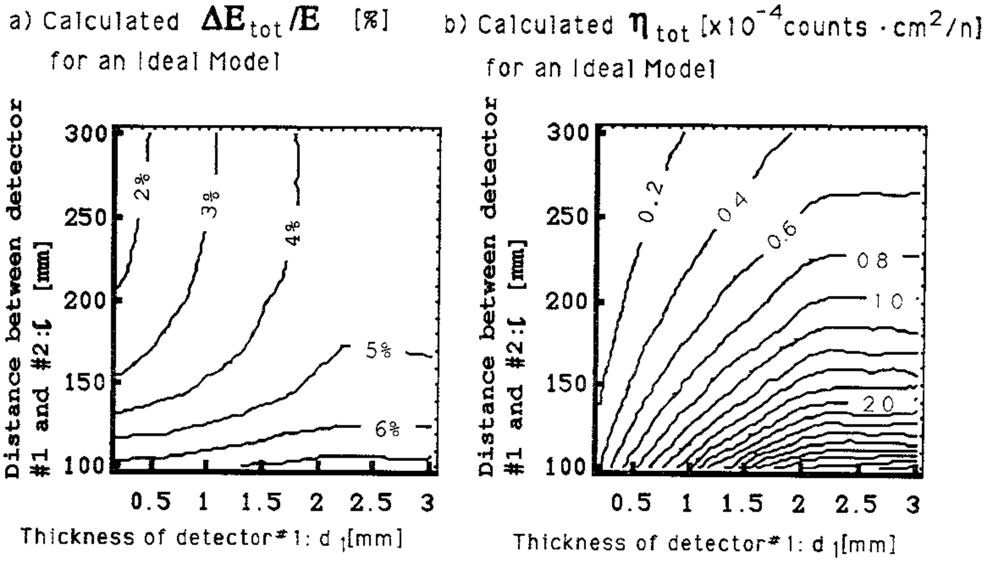

a) Calculated $\Delta E_{tot}/E$ [%] for an Ideal Model

b) Calculated η_{tot} [$\times 10^{-4}$ counts $\cdot$ cm^2/n] for an Ideal Model

Fig.3 Change of the energy resolution and the detection efficiency vs the thickness(d_1) of the detector and the distance between detector #1 and #2(ℓ)

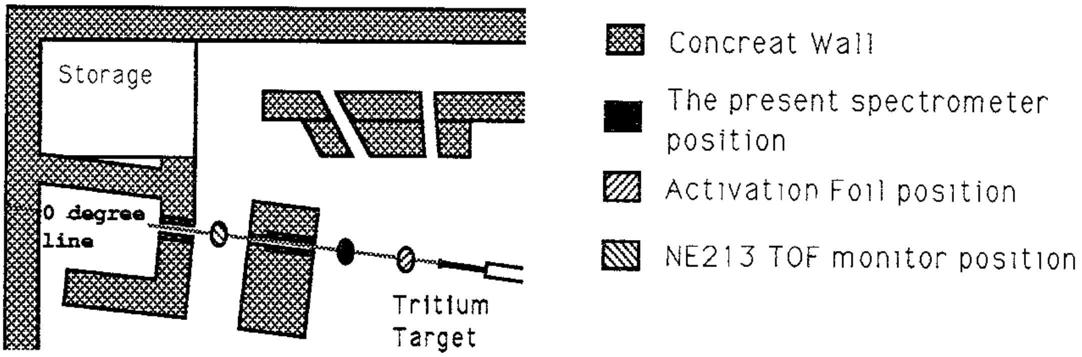

Fig. 4 Schematic layout of the experimental set up. The distances from the present spectrometer, activation foil and TOF monitor to the T target are 141cm, 21cm and 646cm, respectively.

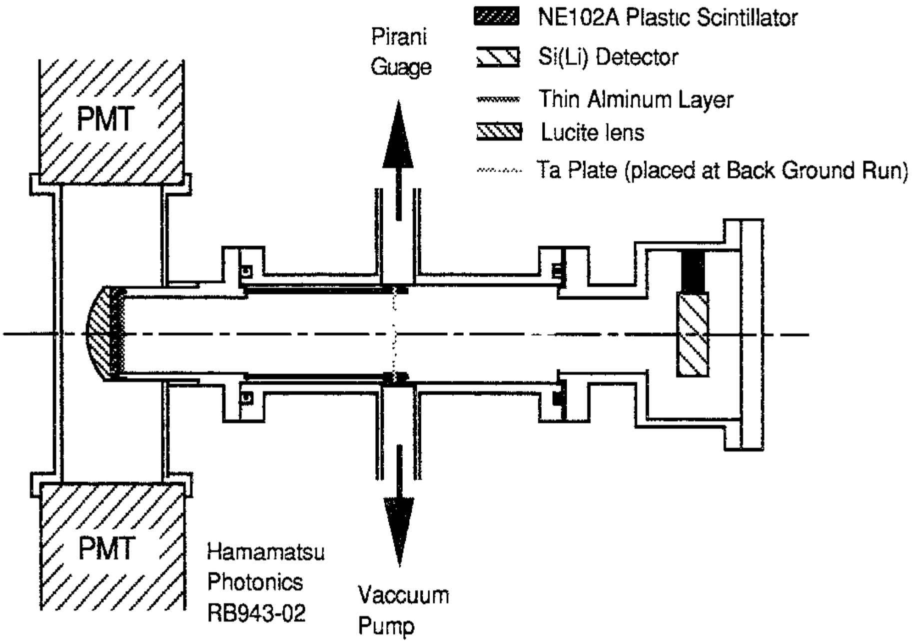

Fig.5 Schematic drawing of prototype spectrometer assembly. Each Chamber can be changeable in accordance with our purpose of measurement.

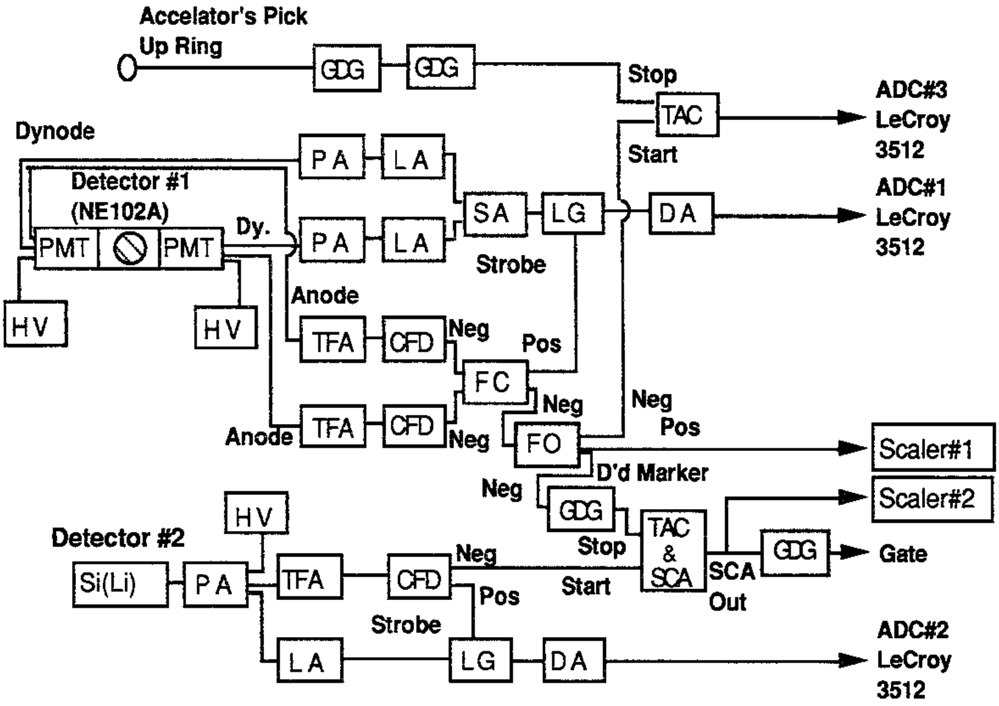

Fig.6 A block diagram of the spectrometer electronic system

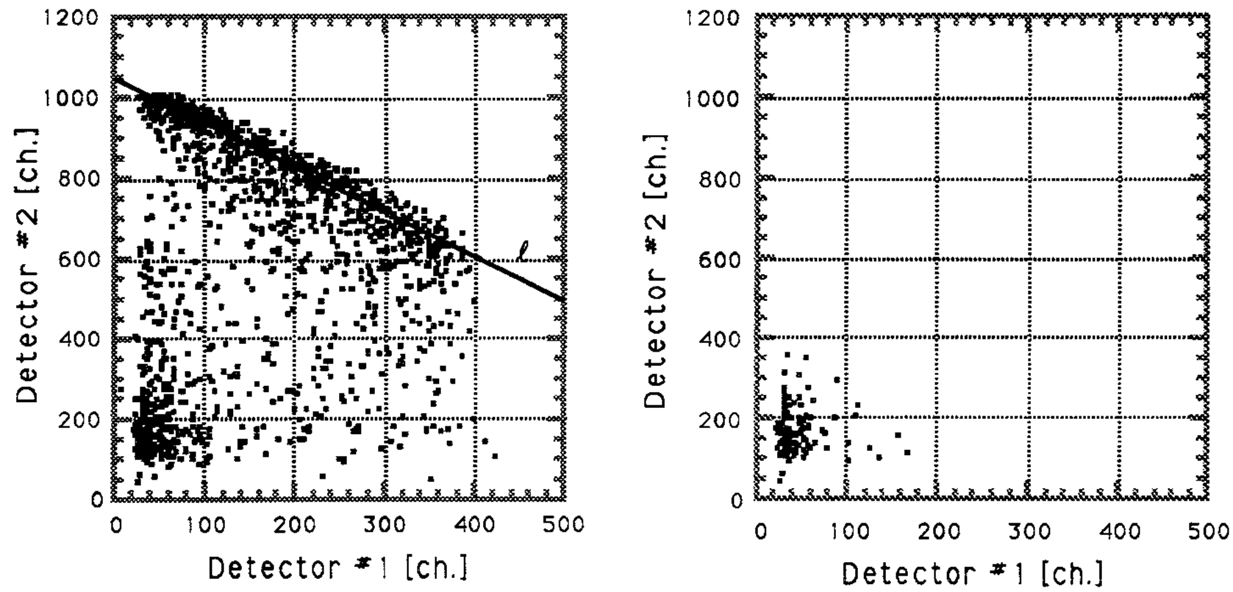

a) Foreground total events

b) Foreground gamma ray events

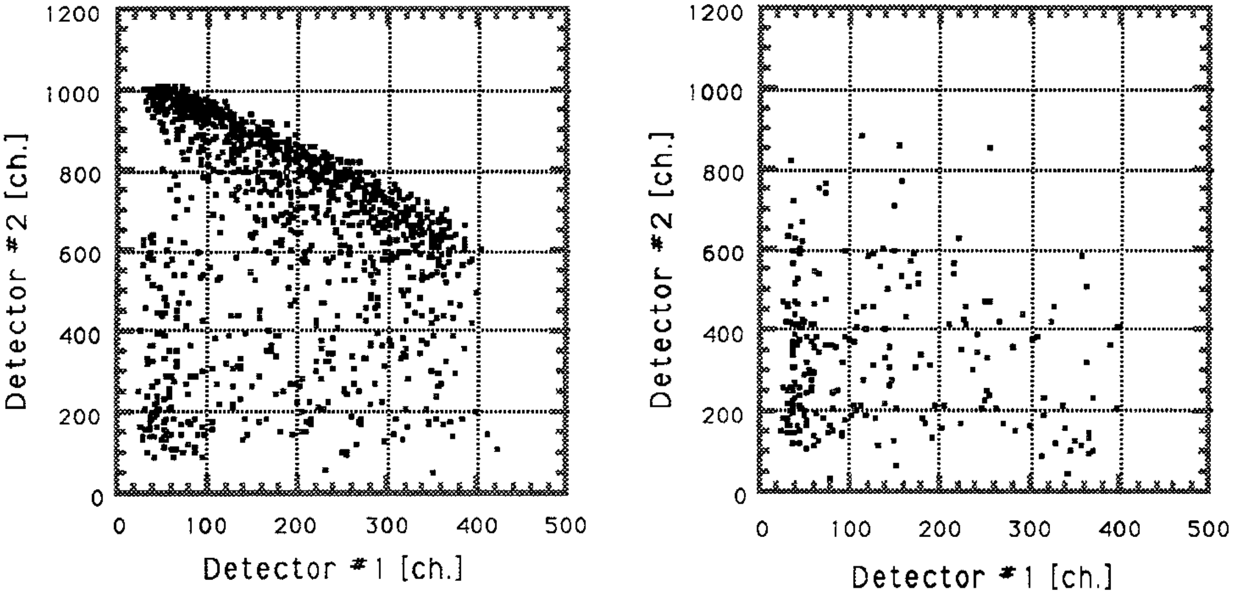

c) Foreground neutron events

d) Background neutron events

Fig. 7 Obtained (L1,L2) distribution. Because of the walk of the timing signals from the PMTs in the detector #1, the higher portion of the L1 signal were lossed. The distibutions (a),(b) and (c) are obtained through the foreground run. The distribution (a) are due to whole events, (b) to γ-ray events, and (c) to neutron evnets. The distribution (d) was obtained through background run which express the (L1,L2) distribution due to the accidental coincidence events. The γ-ray events are eliminated in the distribution (d).

a) Foreground

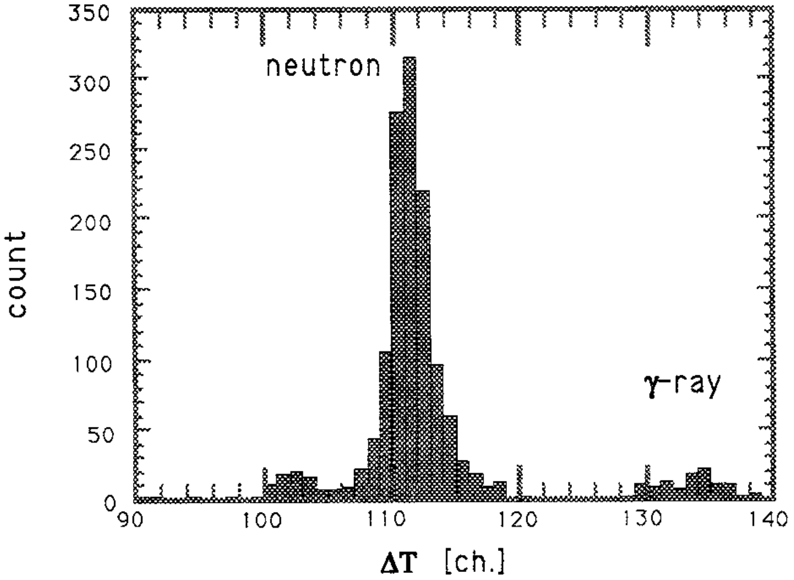

b) Background

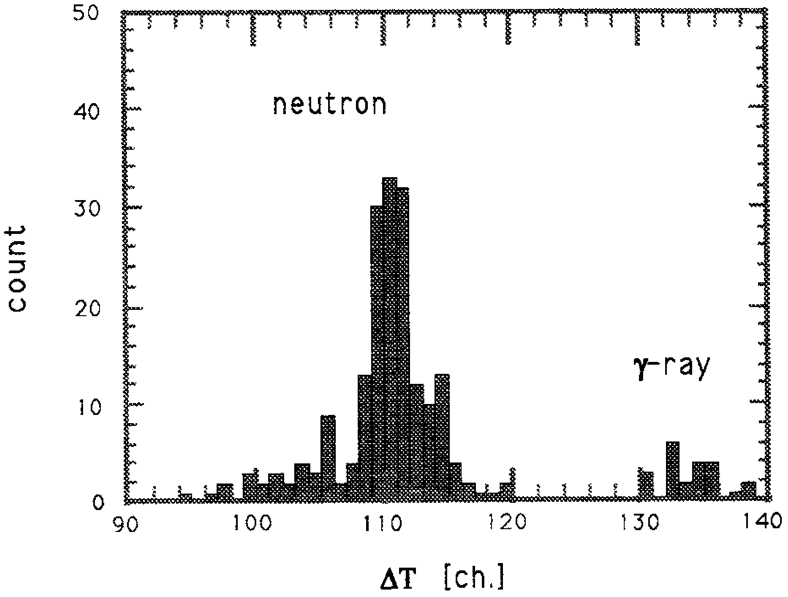

Fig. 8 TOF spectra of neutrons and γ-rays which flew to detector #1 from T target

(a) Foreground

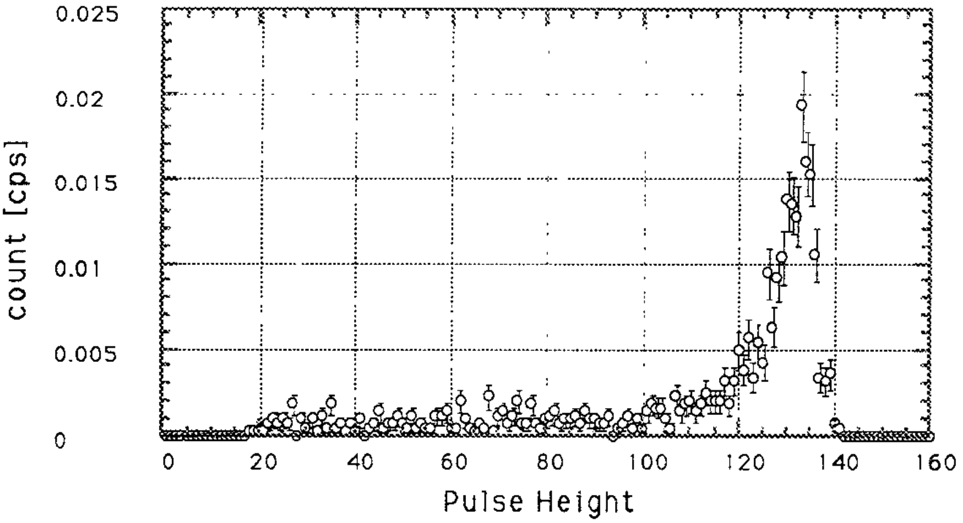

(b) Background

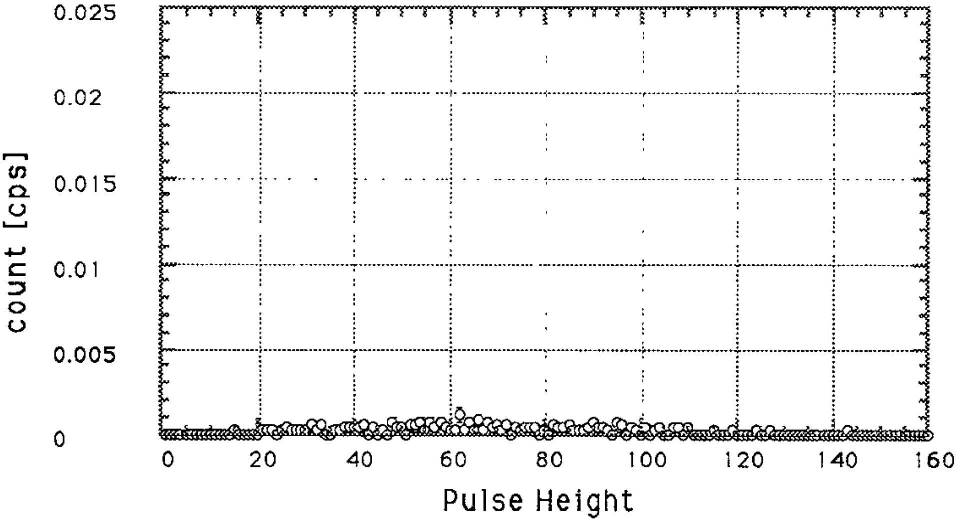

(c) True events

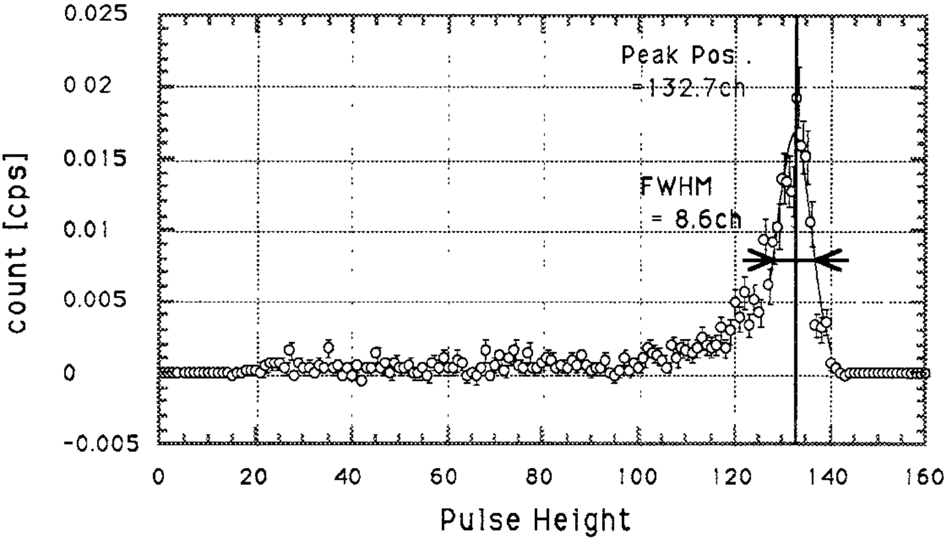

Fig. 9 One dimensional pulse height spectrum of neutron. Both in (a) and (b), the γ-ray events are already removed. The PHS (c) is obtained by subtracting the PHS (b) from (a).

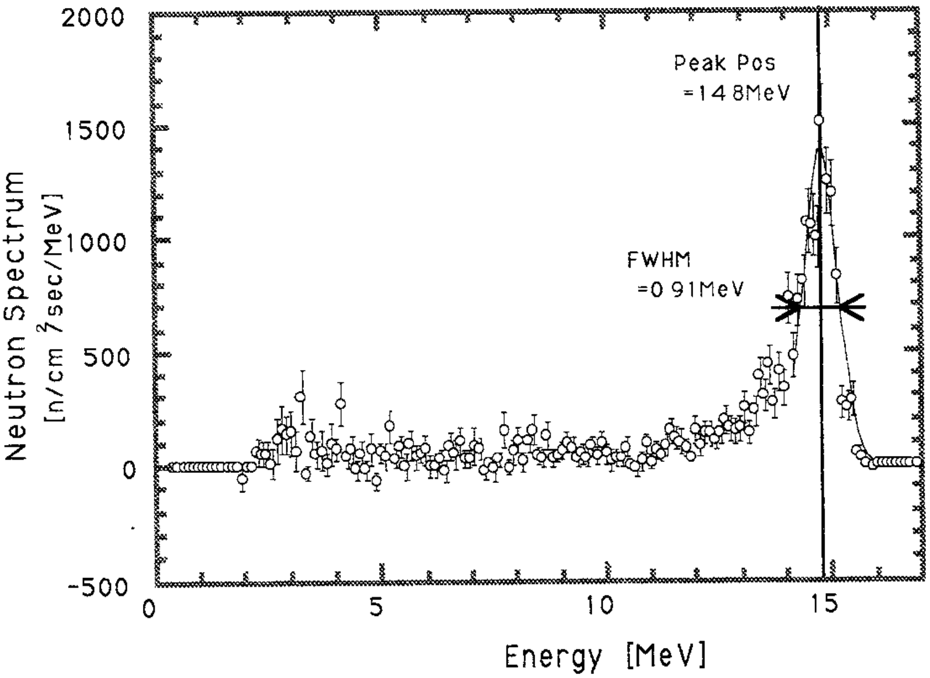

Fig. 10 Obtained Neutron spectrum for DT neutron

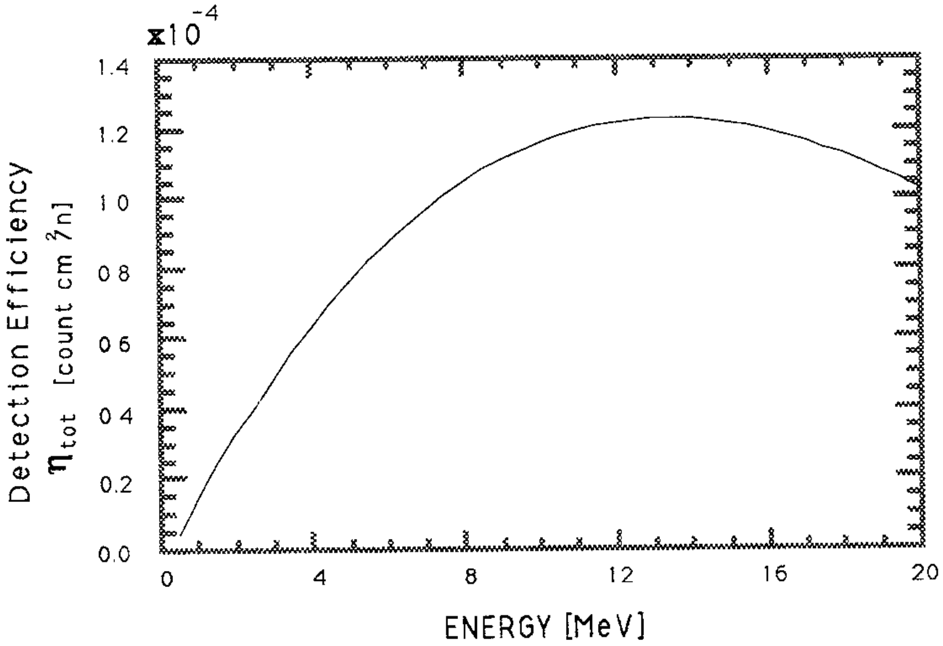

Fig. 11 Calculated detection Efficiency : η_{tot} [count cm ^{2}/n]
The effect of the discrimination on the signal of detector #1 is considered in the calculation.

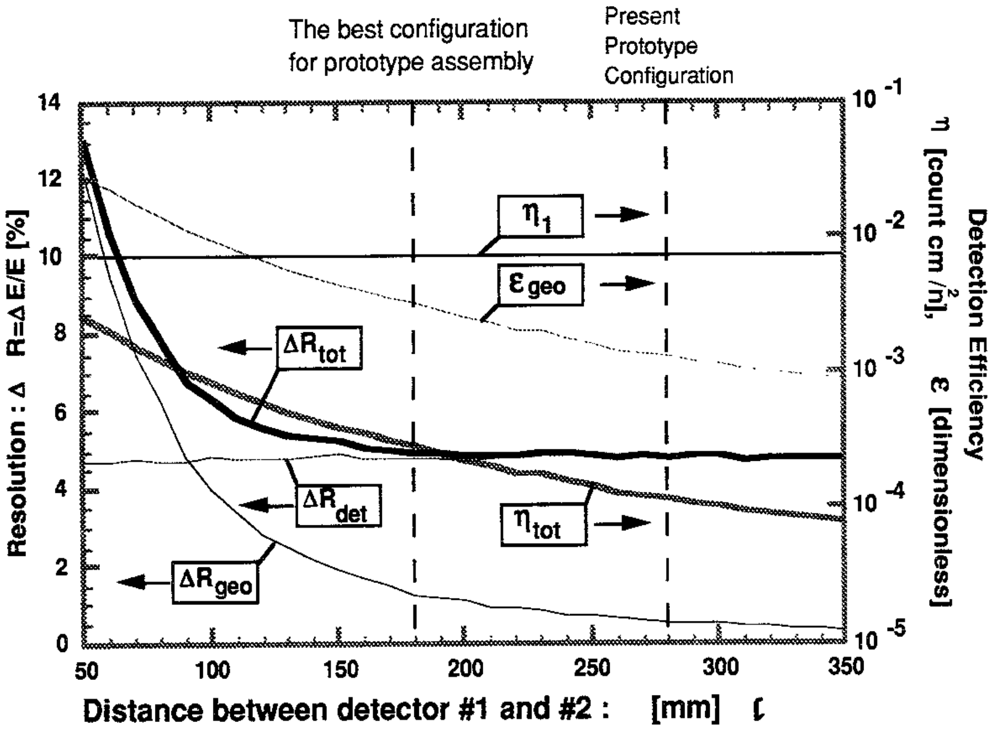

Fig. 12 Breakdowns of the energy resolution and the detction efficiency.

Recent Issues of NIFS Series

NIFS-163 K. Itoh, *A Review on Application of MHD Theory to Plasma Boundary Problems in Tokamaks*; Aug. 1992

NIFS-164 Y.Kondoh and T.Sato, *Thought Analysis on Self-Organization Theories of MHD Plasma*; Aug. 1992

NIFS-165 T. Seki, R. Kumazawa, T. Watari, M. Ono, Y. Yasaka, F. Shimpo, A. Ando, O. Kaneko, Y. Oka, K. Adati, R. Akiyama, Y. Hamada, S. Hidekuma, S. Hirokura, K. Ida, A. Karita, K. Kawahata, Y. Kawasumi, Y. Kitoh, T. Kohmoto, M. Kojima, K. Masai, S. Morita, K. Narihara, Y. Ogawa, K. Ohkubo, S. Okajima, T. Ozaki, M. Sakamoto, M. Sasao, K. Sato, K. N. Sato, H. Takahashi, Y. Taniguchi, K. Toi and T. Tsuzuki, *High Frequency Ion Bernstein Wave Heating Experiment on JIPP T-IIU Tokamak*; Aug. 1992

NIFS-166 Vo Hong Anh and Nguyen Tien Dung, *A Synergetic Treatment of the Vortices Behaviour of a Plasma with Viscosity*; Sep. 1992

NIFS-167 K. Watanabe and T. Sato, *A Triggering Mechanism of Fast Crash in Sawtooth Oscillation*; Sep. 1992

NIFS-168 T. Hayashi, T. Sato, W. Lotz, P. Merkel, J. Nührenberg, U. Schwenn and E. Strumberger, *3D MHD Study of Helias and Heliotron;* Sep. 1992

NIFS-169 N. Nakajima, K. Ichiguchi, K. Watanabe, H. Sugama, M. Okamoto, M. Wakatani, Y. Nakamura and C. Z. Cheng, *Neoclassical Current and Related MHD Stability, Gap Modes, and Radial Electric Field Effects in Heliotron and Torsatron Plasmas;* Sep. 1992

NIFS-170 H. Sugama, M. Okamoto and M. Wakatani, K-ε *Model of Anomalous Transport in Resistive Interchange Turbulence* ; Sep, 1992

NIFS-171 H. Sugama, M. Okamoto and M. Wakatani, *Vlasov Equation in the Stochastic Magnetic Field* ; Sep. 1992

NIFS-172 N. Nakajima, M. Okamoto and M. Fujiwara, *Physical Mechanism of* E_{ϕ}*-Driven Current in Asymmetric Toroidal Systems* ; Sep.1992

NIFS-173 N. Nakajima, J. Todoroki and M. Okamoto, *On Relation between Hamada and Boozer Magnetic Coordinate System* ; Sep. 1992

NIFS-174 K. Ichiguchi, N. Nakajima, M. Okamoto, Y. Nakamura and M. Wakatani, *Effects of Net Toroidal Current on Mercier Criterion* *in the Large Helical Device* ; Sep. 1992

NIFS-175 S. -I. Itoh, K. Itoh and A. Fukuyama, *Modelling of ELMs and Dynamic Responses of the H-Mode* ; Sep. 1992

NIFS-176 K. Itoh, S.-I. Itoh, A. Fukuyama, H. Sanuki, K. Ichiguchi and J. Todoroki, *Improved Models of β-Limit, Anomalous Transport and Radial Electric Field with Loss Cone Loss in Heliotron / Torsatron* ; Sep. 1992

NIFS-177 N. Ohyabu, K. Yamazaki, I. Katanuma, H. Ji, T. Watanabe, K. Watanabe, H. Akao, K. Akaishi, T. Ono, H. Kaneko, T. Kawamura, Y. Kubota, N. Noda, A. Sagara, O. Motojima, M. Fujiwara and A. Iiyoshi, *Design Study of LHD Helical Divertor and High Temperature Divertor Plasma Operation* ; Sep. 1992

NIFS-178 H. Sanuki, K. Itoh and S.-I. Itoh, *Selfconsistent Analysis of Radial Electric Field and Fast Ion Losses in CHS Torsatron / Heliotron* ; Sep. 1992

NIFS-179 K. Toi, S. Morita, K. Kawahata, K. Ida, T. Watari, R. Kumazawa, A. Ando, Y. Oka, K. Ohkubo, Y. Hamada, K. Adati, R. Akiyama, S. Hidekuma, S. Hirokura, O. Kaneko, T. Kawamoto, Y. Kawasumi, M. Kojima, T. Kuroda, K. Masai, K. Narihara, Y. Ogawa, S. Okajima, M. Sakamoto, M. Sasao, K. Sato, K. N. Sato, T. Seki, F. Shimpo, S. Tanahashi, Y. Taniguchi, T. Tsuzuki, *New Features of L-H Transition in Limiter H-Modes of JIPP T-IIU* ; Sep. 1992

NIFS-180 H. Momota, Y. Tomita, A. Ishida, Y. Kohzaki, M. Ohnishi, S. Ohi, Y. Nakao and M. Nishikawa, *D-^{3}He Fueled FRC Reactor "Artemis-L"* ; Sep. 1992

NIFS-181 T. Watari, R. Kumazawa, T. Seki, Y. Yasaka, A. Ando, Y. Oka,O. Kaneko, K. Adati, R. Akiyama, Y. Hamada, S. Hidekuma, S. Hirokura, K. Ida, K. Kawahata, T. Kawamoto, Y. Kawasumi, S. Kitagawa, M. Kojima, T. Kuroda, K. Masai, S. Morita, K. Narihara, Y. Ogawa, K. Ohkubo, S. Okajima, T. Ozaki, M. Sakamoto, M. Sasao, K. Sato, K. N. Sato, F.Shimpo, H. Takahashi, S. Tanahasi, Y. Taniguchi, K. Toi, T. Tsuzuki and M. Ono, *The New Features of Ion Bernstein Wave Heating in JIPP T-IIU Tokamak ;*Sep, 1992

NIFS-182 K. Itoh, H. Sanuki and S.-I. Itoh, *Effect of Alpha Particles on Radial Electric Field Structure in Torsatron / Heliotron Reactor*; Sep. 1992

NIFS-183 S. Morimoto, M. Sato, H. Yamada, H. Ji, S. Okamura, S. Kubo, O. Motojima, M. Murakami, T. C. Jernigan, T. S. Bigelow, A. C. England, R. S. Isler, J. F. Lyon, C. H. Ma, D. A. Rasmussen, C. R. Schaich, J. B. Wilgen and J. L. Yarber, *Long Pulse Discharges Sustained by Second Harmonic Electron Cyclotron Heating Using a*

$35GH_Z$ Gyrotron in the Advanced Toroidal Facility; Sep. 1992

NIFS-184 S. Okamura, K. Hanatani, K. Nishimura, R. Akiyama, T. Amano, H. Arimoto, M. Fujiwara, M. Hosokawa, K. Ida, H. Idei, H. Iguchi, O. Kaneko, T. Kawamoto, S. Kubo, R. Kumazawa, K. Matsuoka, S. Morita, O. Motojima, T. Mutoh, N. Nakajima, N. Noda, M. Okamoto, T. Ozaki, A. Sagara, S. Sakakibara, H. Sanuki, T. Seki, T. Shoji, F. Shimbo, C. Takahashi, Y. Takeiri, Y. Takita, K. Toi, K. Tsumori, M. Ueda, T. Watari, H. Yamada and I. Yamada, *Heating Experiments Using Neutral Beams with Variable Injection Angle and ICRF Waves in CHS* ; Sep. 1992

NIFS-185 H. Yamada, S. Morita, K. Ida, S. Okamura, H. Iguchi, S. Sakakibara, K. Nishimura, R. Akiyama, H. Arimoto, M. Fujiwara, K. Hanatani, S. P. Hirshman, K. Ichiguchi, H. Idei, O. Kaneko, T. Kawamoto, S. Kubo, D. K. Lee, K. Matsuoka, O, Motojima, T. Ozaki, V. D. Pustovitov, A. Sagara, H. Sanuki, T. Shoji, C. Takahashi, Y. Takeiri, Y. Takita, S. Tanahashi, J. Todoroki, K. Toi, K. Tsumori, M. Ueda and I. Yamada, *MHD and Confinement Characteristics in the High-β Regime on the CHS Low-Aspect-Ratio Heliotron / Torsatron* ; Sep. 1992

NIFS-186 S. Morita, H. Yamada, H. Iguchi, K. Adati, R. Akiyama, H. Arimoto, M. Fujiwara, Y. Hamada, K. Ida, H. Idei, O. Kaneko, K. Kawahata, T. Kawamoto, S. Kubo, R. Kumazawa, K. Matsuoka, T. Morisaki, K. Nishimura, S. Okamura, T. Ozaki, T. Seki, M. Sakurai, S, Sakakibara, A. Sagara, C. Takahashi, Y. Takeiri, H. Takenaga, Y. Takita, K. Toi, K. Tsumori, K. Uchino, M. Ueda, T. Watari, I. Yamada, *A Role of Neutral Hydrogen in CHS Plasmas with Reheat and Collapse and Comparison with JIPP T-IIU Tokamak Plasmas* ; Sep. 1992

NIFS-187 K. Ioth, S.-I. Itoh, A. Fukuyama, M. Yagi and M. Azumi, *Model of the L-Mode Confinement in Tokamaks* ; Sep. 1992

NIFS-188 K. Itoh, A. Fukuyama and S.-I. Itoh, *Beta-Limiting Phenomena in High-Aspect-Ratio Toroidal Helical Plasmas*; Oct. 1992

NIFS-189 K. Itoh, S. -I. Itoh and A. Fukuyama, *Cross Field Ion Motion at Sawtooth Crash* ; Oct. 1992

NIFS-190 N. Noda, Y. Kubota, A. Sagara, N. Ohyabu, K. Akaishi, H. Ji, O. Motojima, M. Hashiba, I. Fujita, T. Hino, T. Yamashina, T. Matsuda, T. Sogabe, T. Matsumoto, K. Kuroda, S. Yamazaki, H. Ise, J. Adachi and T. Suzuki, *Design Study on Divertor Plates of Large Helical Device (LHD)* ; Oct. 1992

NIFS-191 Y. Kondoh, Y. Hosaka and K. Ishii, *Kernel Optimum Nearly-Analytical Discretization (KOND) Algorithm Applied to Parabolic and*

Hyperbolic Equations : Oct. 1992

NIFS-192 K. Itoh, M. Yagi, S.-I. Itoh, A. Fukuyama and M. Azumi, *L-Mode Confinement Model Based on Transport-MHD Theory in Tokamaks* ; Oct. 1992

NIFS-193 T. Watari, *Review of Japanese Results on Heating and Current Drive* ; Oct. 1992

NIFS-194 Y. Kondoh, *Eigenfunction for Dissipative Dynamics Operator and Attractor of Dissipative Structure* ; Oct. 1992

NIFS-195 T. Watanabe, H. Oya, K. Watanabe and T. Sato, *Comprehensive Simulation Study on Local and Global Development of Auroral Arcs and Field-Aligned Potentials* ; Oct. 1992

NIFS-196 T. Mori, K. Akaishi, Y. Kubota, O. Motojima, M. Mushiaki, Y. Funato and Y. Hanaoka, *Pumping Experiment of Water on B and* LaB_6 *Films with Electron Beam Evaporator* ; Oct., 1992

NIFS-197 T. Kato and K. Masai, *X-ray Spectra from Hinotori Satellite and Suprathermal Electrons* ; Oct. 1992

NIFS-198 K. Toi, S. Okamura, H. Iguchi, H. Yamada, S. Morita, S. Sakakibara, K. Ida, K. Nishimura, K. Matsuoka, R. Akiyama, H. Arimoto, M. Fujiwara, M. Hosokawa, H. Idei, O. Kaneko, S. Kubo, A. Sagara, C. Takahashi, Y. Takeiri, Y. Takita, K. Tsumori, I. Yamada and H. Zushi, *Formation of H-mode Like Transport Barrier in the CHS Heliotron / Torsatron* ; Oct. 1992

NIFS-199 M. Tanaka, *A Kinetic Simulation of Low-Frequency Electromagnetic Phenomena in Inhomogeneous Plasmas of Three-Dimensions* ; Nov. 1992

NIFS-200 K. Itoh, S.-I. Itoh, H. Sanuki and A. Fukuyama, *Roles of Electric Field on Toroidal Magnetic Confinement*, Nov. 1992

NIFS-201 G. Gnudi and T. Hatori, *Hamiltonian for the Toroidal Helical Magnetic Field Lines in the Vacuum*; Nov. 1992

NIFS-202 K. Itoh, S.-I. Itoh and A. Fukuyama, *Physics of Transport Phenomena in Magnetic Confinement Plasmas*; Dec. 1992

NIFS-203 Y. Hamada, Y. Kawasumi, H. Iguchi, A. Fujisawa, Y. Abe and M. Takahashi, *Mesh Effect in a Parallel Plate Analyzer*; Dec. 1992

NIFS-204 T. Okada and H. Tazawa, *Two-Stream Instability for a Light Ion Beam -Plasma System with External Magnetic Field;* Dec. 1992